Published in final edited form as:

Nature. 2024 August ; 632(8024): 437–442. doi:10.1038/s41586-024-07637-0.

Mechanisms of actin filament severing and elongation by formins

Nicholas J. Palmer[1], **Kyle R. Barrie**[1], **Roberto Dominguez**[1]

[1]Department of Physiology and Biochemistry and Molecular Biophysics Graduate Group, University of Pennsylvania Perelman School of Medicine, Philadelphia, Pennsylvania, USA

Abstract

Humans express fifteen formins, playing crucial roles in actin-based processes, such as cytokinesis, cell motility, and mechanotransduction [1,2]. However, the lack of structures bound to the actin filament (F-actin) has been a major impediment to understanding formin function. While formins are known for their ability to nucleate and elongate F-actin [3–7], some formins can additionally depolymerize, sever, or bundle F-actin. Two mammalian formins, inverted formin-2 (INF2) and diaphanous-1 (Dia1), exemplify this diversity. INF2 displays potent severing activity but elongates weakly [8–11], whereas Dia1 has potent elongation activity but does not sever [4,8]. Using cryo-electron microscopy (cryo-EM), we reveal five structural states of INF2 and two of Dia1 bound to the middle and barbed end of F-actin. INF2 and Dia1 bind differently to these sites, consistent with their distinct activities. The FH2 and WH2 domains of INF2 are positioned to sever F-actin, whereas Dia1 appears unsuited for severing. Structures also show how profilin-actin is delivered to the fast-growing barbed end, and how this is followed by a transition of the incoming monomer into the F-actin conformation and the release of profilin. Combined, the seven structures presented here provide step-by-step visualization of the mechanisms of F-actin severing and elongation by formins.

The formin family of proteins is encoded by fifteen genes in humans, divided into eight subclasses based on phylogenetic analysis [12] and domain organization [1]. Because of their ability to nucleate and elongate F-actin, formins can assemble structures consisting of linear filaments and bundles, such as stress fibers, filopodia, and the cytokinetic ring. Accordingly, formins play essential roles in processes such as cytokinesis, cell motility, tissue morphogenesis, mitochondrial fission, and mechanotransduction, and have been linked to pathologies ranging from cardiomyopathies and cancers to neurological disorders [1,2,11,13,14].

Correspondence and requests for materials should be addressed to Roberto Dominguez (droberto@pennmedicine.upenn.edu).

Author contributions: N.J.P. and K.R.B. and R.D. conceived and designed the study. N.J.P. performed sample preparation and cryo-EM data collection. N.J.P. and K.R.B. processed the cryo-EM data and generated 3D reconstructions. N.J.P. and K.R.B. and R.D. conducted structural analyses and interpretations. N.J.P. and K.R.B. and R.D. prepared figures and videos. R.D. wrote the initial draft, acquired funding, and supervised the work. N.J.P. and K.R.B. and R.D. edited the final manuscript.

Competing interests: The authors declare no competing interests.

Additional information

Supplementary information: The online version contains supplementary material

Despite their diverse domain architectures, all formins feature adjacent formin-homology domains 1 and 2 (FH1 and FH2). The FH1 comprises a varying number of Pro-rich segments that bind profilin–actin, the main source of actin monomers (G-actin) for F-actin assembly in cells [4,15]. The FH2 forms a dimeric, ring-like structure through head-to-tail interaction of its two subunits [16]. This domain promotes nucleation by recruiting two actin monomers in an orientation resembling the short-pitch helix of F-actin [5] (Extended Data Fig. 1 illustrates nomenclatures used). The FH2 also acts as a "leaky" cap, allowing for monomer addition and dissociation while remaining bound at the barbed end [4,17]. Together, the FH1 and FH2 constitute the minimal region necessary and sufficient for processive barbed end elongation from profilin-actin [3,18]. In some formins, sequences C-terminal to the FH2 enhance nucleation by recruiting G-actin directly [8,19] or indirectly through proteins that bind G-actin [20,21]. Other formin domains are less conserved and are typically involved in regulation and subcellular localization.

Crystal structures of various formin domains, including the FH2 in complex with G-actin, have led to different models of elongation [5–7]. However, the lack of structures bound to F-actin has been a major obstacle to understanding formin function. Moreover, formins differ widely in their ability to nucleate and elongate F-actin, and some formins can additionally depolymerize, sever, or bundle F-actin. Accounting for this functional diversity, we study here two mammalian formins, INF2 and Dia1, displaying potent F-actin severing [8,9] and elongation [4] activities, respectively. INF2 plays an essential role in mitochondrial fission [11] and Dia1 is implicated in the formation of stress fibers, the contractile ring, and cell migration [22–24]. Mutations in INF2 cause focal segmental glomerulosclerosis [25] and Charcot-Marie-Tooth neuropathy [26] whereas mutations in Dia1 cause deafness [27]. The cryo-EM structures of INF2 and Dia1 illuminate the mechanisms of severing and processive elongation from profilin-actin and show how different formins specialize in distinct activities.

Formin structures bound to F-actin

Structures of INF2 and Dia1 were determined using single-particle cryo-EM. To enhance the number of barbed ends per micrograph, different sample preparation strategies were optimized for each formin. Because INF2 favors mid-filament binding and severing, the emphasis was on redirecting part of its population to the barbed end, requiring the addition of profilin-actin and the presence of the FH1, FH2, and C-terminal tail [10]. With Dia1, which favors barbed end elongation, the FH1 and profilin were not included and the number of barbed ends was increased through mechanical shearing. This strategy resulted in seven structural states being observed, including two states of INF2 and one of Dia1 bound to the middle of F-actin and three states of INF2 and one of Dia1 at the barbed end (Fig. 1, Extended Data Fig. 2, Extended Data Table 1–2, Supplementary Figs. S1–14). For INF2, including the FH1 and profilin-actin led to barbed end-bound structures of this formin alone and with incoming profilin-actin or actin.

While the global resolution of the maps ranged from 3.0 to 3.8 Å, these values were dominated by F-actin, which was well defined in all the maps. The F-actin portion of the structures comprised six subunits, denoted A1 to A6 from pointed to barbed end along the

short-pitch helix (Fig. 1). Actin subunits had ADP bound and displayed the typical flat conformation and positioning of subunits in free F-actin, except A6 at the formin-bound barbed end, which was slightly rotated (below).

The formins were resolved at lower resolution, and only the FH2s of both formins and the WH2s of INF2 were visualized (Fig. 1). Traditionally, the FH2 has been described as consisting of five subdomains: lasso, linker, knob, coiled-coil, and post [16]. Because of its prominent role in severing and elongation, we introduced here a new element, the antenna, corresponding to the long C-terminal helix of the FH2 (Extended Data Fig. 1a–b). In the dimer, the lasso of one subunit binds the post of the other subunit in a head-to-tail fashion to close the ring. In the structures, the knob, lasso-post, and antenna accounted for most of the contacts with F-actin (Extended Data Fig. 3 illustrates contact surface areas). Overall, however, the FH2 appeared loosely associated with F-actin in all the states, likely explaining why it was less well-resolved in the maps. While the α-helices that characterize the FH2 fold were well defined, side chains were frequently not observed and were assigned the rotamer orientation suggested by AlphaFold [28]. The lower resolution of the FH2 in the maps is not due to limitations of the single-particle approach used, which has yielded high-resolution structures of other targets [29], but may instead hold functional significance, reflecting the ability of this domain to rapidly explore a range of states during severing and elongation.

Binding to the middle of F-actin

Both formins were more frequently found at the middle than at the barbed end of F-actin. Of the total number of particles in the final reconstructions, 76% of INF2 and 62% of Dia1 corresponded to mid-filament bound states (Extended Data Tables 1 and 2). INF2's preference for mid-filament binding is striking, particularly considering that its presence at the barbed end may often follow a severing event, after binding first to the middle [9].

Each filament has a single barbed end- but multiple mid-filament-binding sites, which may in part explain the prevalence of mid-filament bound states. Yet, mid-filament binding may proceed through different mechanisms for different formins: a) sliding from the barbed end, b) end-to-end filament annealing, and c) opening of the FH2 ring after dissociation of the lasso-post interaction. Sliding along F-actin has been observed with DAAM1 [30] and Dia1 [31], but for the latter only in the presence of capping protein, which competes for binding to the barbed end. Sliding entails a high energy cost [31], suggesting it may not be the prevalent mechanism explaining our observations. Filament annealing likely depends on how tightly a formin binds to the barbed end; it is inhibited with Cdc12, which caps the barbed end in the absence of profilin 18, but may occur with Dia1, which binds the barbed end more dynamically [3] and whose elongation rate in the absence of profilin is similar to that of F-actin alone [4]. INF2 falls in between these two formins, allowing for some monomer addition in the absence of profilin [10]. Dia1 and INF2 also represent opposite ends of the lasso-post dissociation spectrum, with Dia1 undergoing little dissociation [32] and INF2 dissociating readily [9]. Based on these considerations, INF2 and Dia1 are likely to bind the middle mainly through lasso-post dissociation and filament annealing, respectively.

INF2 exhibited two distinct binding states in the middle of F-actin (Fig. 1b,c). In both states, one FH2 of the dimer occupied a similar position (static), while the other FH2 (mobile) assumed down (toward the barbed end, Fig. 1b) or up (toward the pointed end, Fig. 1c) states. Between states, the mobile FH2 underwent a rotation centered on the lasso-post, causing the coiled-coil and knob to swing ~29° (Supplementary Video 1). In the up state, the FH2 dimer contacted three actin subunits (A3, A4, A5), whereas in the down state it contacted four (A3, A4, A5, A6). The flexible lasso-knob linkers, not observed in the maps, likely allowed the transition between states, with the rest of the FH2 moving mostly as a rigid body.

In the down state, the two FH2 subunits bound pseudo-symmetrically, making similar contacts on each side of F-actin. The knob of the static FH2 bound at the interface of A3 and A5 (Fig. 1b, Extended Data Figs. 2 and 3, Supplementary Video 1). In crystal structures of FH2 complexes with G-actin [5,7], a helix in the knob (INF2 residues A635-F648) binds in the hydrophobic cleft (H-cleft) between actin subdomains 1 and 3. This helix plays a central role in the interaction with F-actin, and was named here the H-cleft-binding helix (HCBH, Extended Data Fig. 1). In F-actin, the H-cleft participates in inter-subunit contacts, with the cleft of A3 being occupied by the D-loop of A5 (Fig. 2). Consequently, the HCBH interacted with the D-loop of A5 and faced but did not engage the H-cleft of A3 (Fig. 2 and Extended Data Figs. 2h and 3). A conserved residue within the HCBH, I643 (INF2 numbering), is functionally essential in several formins [7,16,32–34], including INF2 where the I643A mutation inhibits severing [34]. Other contacts of the static FH2 implicated the antenna and a loop within the post (L786-L800), which both contacted subdomain 1 of A4 and subdomain 4 of A5 (Extended Data Fig. 3). Within this loop, mutations of the residue corresponding to INF2 K792 reduce actin polymerization in several formins [7,16,33,34]. In the down state, the mobile FH2 made similar contacts on the opposite side of F-actin, with its knob facing the H-cleft of A4 and the D-loop of A6, and the post and antenna contacting subdomain 1 of A3 and subdomain 4 of A4 (Fig 1b and Fig. 2a, Extended Data Figs. 2–3).

In the up state, the FH2s of INF2 bound asymmetrically. The static FH2 made similar contacts as in the down state. Because the post of the mobile FH2 remained approximately in the same position during the up-down rotation, it also made similar contacts with subdomain 1 of A3 and subdomain 4 of A4 as in the down state (Fig 1c, Extended Data Figs. 2g–h and 3). However, the knob of the mobile FH2 no longer faced the H-cleft of A4 but instead faced subdomain 1 of A4 (Extended Data Fig. 2h and 3). Between up and down states, HCBH residue I643 moved ~25 Å, i.e. approximately half a protomer length.

In the middle of F-actin, Dia1 appeared more loosely associated and less well-defined than INF2, adopting a single conformation distinct from both states of INF2 (Fig. 1d). Like the down state of INF2, Dia1 bound pseudo-symmetrically. One FH2 subunit occupied approximately the same position as the static FH2 of INF2, albeit rotated toward the pointed end by ~10° (rotation centered on the HCBH, Supplementary Video 1). The knob of this FH2 contacted the H-cleft of A3 and the D-loop of A5. The knob of the other FH2 made similar contacts with A2 and A4. This contrasted with the down state of INF2, where the knob of the mobile FH2 contacted the H-cleft of A4 and the D-loop of A6, i.e. one actin subunit down along the long-pitch helix (Fig. 1b,d and Supplementary Video 1). Contrary

to INF2, other subdomains of Dia1's FH2 mostly did not contact F-actin, except a minor interaction involving the loop K989-L1002 (mouse Dia1 numbering) (Extended Data Fig. 3). A mid-filament bound state of Dia1 was previously observed using negative stain EM [35], but could not be compared to the current structure due to the limited resolution of that study.

Binding of INF2's WH2 to F-actin

Individually, the FH2 and WH2 of INF2 have weak and no severing activity, respectively, but together they synergize to achieve severing activity surpassing that of cofilin [9]. The structures suggest how this may be achieved by INF2 but not Dia1. In both states of INF2, the WH2s bound to a site adjacent to the H-cleft on subdomain 1 of A1 and A2, immediately above the actin subunits binding the FH2s (Fig. 1b,c, Fig. 2a, and Supplementary Video 1). In contrast, Dia1's WH2, also called the diaphanous autoregulatory domain (DAD) due to its dual role in autoinhibition and nucleation [19], was not observed. For Dia1, the binding site on A2 was occluded by the knob of the FH2 closer to the pointed end (Fig. 1d), but this did not explain why the other WH2 was not observed on A1. The reason may lie in the length and orientation of the antennas, which pointed away from F-actin. According to AlphaFold, Dia1's antenna is 11 amino acids longer (three helical turns) than INF2's, whereas the linker between the antenna and WH2 is shorter in Dia1 than in INF2 (12 vs. 22 amino acids) (Extended Data Fig. 4). As a result, the predicted distance between the end of the antenna and the start of the WH2 was ~45 Å for Dia1 and ~30 Å for INF2, allowing the WH2 of INF2 but not Dia1 to bind F-actin.

Hand-over-hand severing mechanism

In crystal structures, the WH2 binds in the H-cleft of G-actin [36], which is also the binding site predicted by AlphaFold [28] for the canonical WH2 of INF2 (Fig. 2b and Extended Data Fig. 4a). It thus appears that the WH2 of INF2 can bind to two adjacent sites, targeting the site in subdomain 1 when its more favorable binding site in the H-cleft is occupied by the D-loop in F-actin. This suggested a hand-over-hand severing mechanism. Thermal motions of the D-loop may allow the WH2 to competitively bind the H-clefts of A1 and/or A2, weakening inter-subunit contacts along the long-pitch helix (Fig. 2 and Supplementary Video 2). This initial step may then enable the FH2 to engage the H-clefts of the subunits immediately below (A3 and/or A4). Thermal motions then break the remaining weak lateral contacts of the two long-pitch helices, severing the filament. In the down state, this sequence of events may happen on either side of F-actin, since the knob of both FH2s face the H-cleft, whereas in the up state only the static FH2 is properly positioned to engage the H-cleft. When the FH2 engages the H-cleft, its conformation becomes that observed at the barbed end (below).

The WH2 of Dia1 lacks the canonical LKKT motif (^{986}LRKT^{989} in INF2), essential for binding to G-actin [37] (Extended Data Fig. 4a) and may not be able to compete with the D-loop for binding to the H-cleft. Therefore, INF2 seems to have acquired robust severing activity through several adaptations that distinguish it from Dia1: a) weaker lasso-post interaction favoring mid-filament binding, b) shorter antenna and longer antenna-WH2 linker enabling WH2 binding to F-actin, c) canonical WH2 capable of competing with the

D-loop for binding to the H-cleft, d) tighter association of the FH2 with the middle of F-actin, and e) HCBH capable of competing with the D-loop for binding to the H-cleft. At the barbed end, some of these adaptations may hinder elongation.

Binding to the barbed end

Dia1 is the fastest elongating formin studied [4] whereas INF2 is one of the slowest [10]. Differences in their barbed end-bound structures may explain their different elongation activities. In both formins, the FH2s closed in toward the main axis of F-actin, narrowing the aperture of the ring compared to their open conformations in the middle of F-actin (Fig. 1, Extended Fig. 2a–g, Supplementary Video 3). One FH2 engaged the H-cleft of A5 while the other engaged that of A6, referred to as trailing and leading FH2s, respectively (Fig. 3). With both formins, A5 remained mostly unchanged, whereas A6 was rotated away from the main filament axis ~2.5° in INF2 and ~1.5° in Dia1 (rotation centered on the D-loop).

After superimposing the F-actin portion of the structures, the FH2s of the two formins, especially the leading FH2, occupied substantially different positions (Extended Data Fig. 4c–d and Supplementary Video 3). Even greater differences were observed when comparing both formins to crystal structures of the FH2 bound to G-actin [5,7], likely attributable to differences in the interaction with G- vs. F-actin.

In both formins, the knobs accounted for most of the contact surface with A5 and A6 (Extended Data Fig. 3). Minor contacts involved the coiled-coils, which interacted with subdomain 3 of A5 (trailing FH2) and A6 (leading FH2), and the lasso-post of the trailing FH2, which interacted with subdomain 1 of A6. However, the antennas of INF2 made contacts with subdomain 1 of A4 (trailing FH2) and A5 (leading FH2) that were not observed with Dia1. As a result, INF2 had a larger contact surface with the barbed end than Dia1 (2641 $Å^2$ vs. 2176 $Å^2$, Extended Data Fig. 3), suggesting tighter binding. The looser and more dynamic association of Dia1 with the barbed end may, at least in part, explain its fastest elongation rate [3,4].

As observed in the middle of F-actin, the WH2s of INF2 were bound on the side of subdomain 1 of A2 (trailing FH2) and A3 (leading FH2) (Fig. 1e), whereas those of Dia1 were unresolved. The distance from the antenna to the WH2 of INF2 was ~40 Å for the leading FH2 and ~50 Å for the trailing FH2. This is substantially longer than in the middle of F-actin (16 to 33 Å), highlighting the importance of INF2's long and flexible antenna-WH2 linker for WH2 binding to F-actin. The WH2 could play opposite roles in elongation by either helping the FH2s remain bound during processive elongation or imposing a drag on elongation. Generally, features that made INF2 an effective severing protein could negatively impact its elongation rate, including tighter binding to F-actin via the FH2 and WH2 domains, and a higher likelihood of dissociation through severing of terminal barbed end subunits.

Incoming profilin-actin

Profilin-actin was recruited through interactions with the lasso-post of the leading FH2, which contacted both profilin and subdomain 1 of the incoming monomer (Fig. 3b). For

this, the lasso-post moved from its position in the barbed end-bound structure by as much as 18 Å toward the main axis of F-actin, following a rotation centered on the HCBH (Supplementary Video 4). While profilin was likely also bound to the FH1, this interaction was not clearly visualized in the map. The incoming monomer displayed the characteristic "twisted" conformation of G-actin and was additionally rotated 14° compared to its final position in F-actin (Extended Data Fig. 5). The D-loop of the incoming monomer inserted into the H-cleft of A5, dislodging the HCBH of the trailing FH2, consistent with molecular dynamics simulations showing that the D-loop forms the strongest link for terminal subunits at the barbed end [38]. As a result, the trailing FH2 became highly flexible and was only observed at low contour levels of the map (Fig. 1f), contrasting with the barbed end-bound structure where the trailing FH2 was better defined than the leading FH2 (Fig. 1e). After being displaced, the most prevalent position of the trailing FH2 more closely resembled that of the static FH2 in the mid-filament bound states.

G to F transition in incoming actin

In the incoming actin structure, the monomer moved further to occupy its final position in F-actin (Fig. 3e–f and Extended Data Fig. 5). The trailing FH2 remained flexible and occupied approximately the same position as in the profilin-actin structure (Fig. 1g). The leading FH2 was still rotated inward with its lasso-post contacting the incoming monomer (Fig. 3c). Subdomain 2 of the incoming monomer was also similarly positioned, with the D-loop inserted in the H-cleft of A5. However, subdomain 4 now interacted with subdomain 3 of A5 and with subdomain 1 of A6, as in F-actin. These new interactions induced a rotation of subdomains 3 and 4 relative to subdomains 1 and 2 in the incoming monomer, resulting in the flat conformation characteristic of F-actin subunits (Fig. 3e–f). Although this transition readies the catalytic site for ATP hydrolysis [39], we could not verify the nucleotide state at this resolution. The G-to F-actin transition appears to have triggered the dissociation of profilin, which was no longer observed. Indeed, profilin binds in the H-cleft of G-actin, which is substantially remodeled during the G- to F-actin transition, sterically hindering profilin interactions. This offers a structural explanation for the rapid dissociation of profilin from the barbed end during elongation from profilin-actin [40].

This transient association of profilin with the incoming monomer contrasts with a recent study describing formin structures at the barbed end, where a profilin mutant that inhibits elongation (S71M) was stably bound to a barbed end subunit in the F-actin conformation [41]. Differences in sample preparation may explain additional differences between the two studies. Thus, five structures described here were not observed in that study, including mid-filament bound states supporting our severing mechanism, and structures of incoming profilin-actin and actin at the barbed end that led us to a different elongation mechanism.

LERA elongation mechanism

Two elongation models had been proposed: the "stair-stepping" model [5], where the trailing FH2 steps first, opening a binding site for profilin-actin recruitment, and the "stepping second" model 6,7, where profilin-actin joins the barbed end first and the trailing FH2 steps second to stabilize profilin-actin's recruitment. A third, "undock-and-lock" mechanism was

proposed in the study mentioned above [41]. While all the models share features in common, structural intermediates observed here support a different, multi-step elongation model (Fig. 3g and Supplementary Video 4). We named this mechanism LERA (load, exchange, release, and advance): a) as a result of thermal motions, the leading FH2 swings towards the main filament axis to **load** profilin-actin bound to the FH1 [42]. During this step, the FH2 may swing before, during, or after profilin-actin arrives at the barbed end, and its lasso-post contacts both subdomain 1 of the incoming monomer and profilin, revealing an additional role of profilin in formin-mediated elongation, b) the D-loop of the incoming monomer inserts into the H-cleft of the penultimate subunit (A5), **exchanging** with the trailing FH2, which becomes highly flexible. By holding on to profilin-actin, the leading FH2 may both decrease the dissociation rate and enhance the likelihood that the D-loop of the incoming subunit displaces the trailing FH2, c) interactions via subdomain 4 induce a further rotation of the incoming monomer towards its final position in F-actin, triggering the G- to F-actin transition and the **release** of profilin, and d) the trailing FH2 **advances** to engage the H-cleft of the incoming monomer, taking the place of profilin and becoming the new leading FH2, whereas the new trailing FH2 swings back to its barbed end position. This cycle is processively repeated.

Methods

Proteins:

α-Actin and profilin were purified as described [42]. An expression plasmid of GST-fused human $INF2_{469–1249}$ (UniProt Q27J81) was provided by Henry Higgs [10] and transformed into Artic cells, grown in Terrific Broth medium at 37 °C until the OD_{600} reached 1.0–2.0. Expression was induced with 1 mM Isopropylthio-β-D-galactoside (IPTG) and carried out for 22 h at 9 °C. Cells were harvested by centrifugation at 4,000 rpm for 20 min at 4 °C. Pellets from 2 L of cells were pooled and stored at −20 °C. For purification, a 2 L cell pellet was resuspended in 200 mL of 50 mM Tris HCl pH 8.0, 500 mM NaCl, 5 mM EDTA, 1 mM dithiothreitol (DTT), 1 mM phenylmethylsulfonyl fluoride (PMSF), and a protease inhibitor cocktail (Roche), and lysed using a microfluidizer apparatus (Microfluidics). The cell lysate was clarified by centrifugation at 20,000 rpm for 20 min at 4 °C, loaded onto a GST affinity column, and washed with 20 mM Tris HCl pH 8.0, 250 mM NaCl, 1 mM EDTA, 1 mM DTT, 0.05% Thesit, and a protease inhibitor cocktail. INF2 (residues 469–1249) was cleaved from GST with TEV protease overnight and eluted. INF2 was dialyzed overnight in 20 mM Tris HCl pH 8.0, 50 mM NaCl, 1 mM EDTA, 1 mM DTT, and 0.05% Thesit and further purified through a MonoQ ion exchange column (Pharmacia) using a 50–500 mM NaCl gradient in 20 mM Tris HCl pH 8.0, 1 mM EDTA, 1 mM DTT, and 0.05% Thesit. INF2 was dialyzed overnight into 20 mM HEPES pH 8.0, 50 mM NaCl, 1 mM EDTA, 1 mM DTT, and 0.05% Thesit, and spin concentrated to ~70 μM.

The cDNA of mouse Dia1 (UniProt O08808) was a gift from Henry Higgs. MBP-fused construct Dia1 residues 739–1255 was cloned into the pMal vector. Protein expression and purification was carried out as described above for INF2, except using an amylose column for affinity purification and 5% glycerol added to the buffers. Dia1 was concentrated using an ultrafiltration device (Amicon) with an Ultracel 10 kDa ultrafiltration disc (Millipore).

Cryo-EM data collection:

For INF2, 131 μM profilin and 65 μM α-actin were incubated together for 1 h in F-buffer (20 mM HEPES pH 7.5, 50 mM KCl 1mM EGTA, 1mM $MgCl_2$, 1 mM ATP, and 1 mM DTT). INF2 (70 μM) was then added to the profilin-actin solution to final concentrations of 60 μM profilin, 30 μM actin, and 15 μM INF2. The solution was incubated for 10–15 min before vitrification. The sample (3 μL) was applied onto glow-discharged (120 sec, PELCO easiGlow) 300-mesh R1.2/1.3 Quantifoil holey carbon grids (Electron Microscopy Sciences). Grids were blotted for 2.5 sec with force 7 using Whatman 41 filter paper and vitrified by plunging into liquid ethane using a Vitrobot Mark IV.

For Dia1, 37 μM actin was polymerized in F-buffer for 1 h, then sonicated using a Fisher Scientific FS20 Ultrasonic Cleaner for 2 min before adding 80 μM Dia1 to final concentrations of 20 μM actin and 18.4 μM Dia1. Samples (3 μL) were immediately applied onto glow-discharged grids and vitrified as above.

Datasets were collected in multiple sessions using the EPU software (ThermoFisher Scientific) on a FEI Titan Krios transmission electron microscope operating at 300 kV, outfitted with a Gatan K3 direct electron detector with an energy quantum filter. Images were collected in super-resolution mode at a defocus range of −0.5 to −2.5 μm and magnification of 81,000x with a pixel size of 0.54 Å/pix. A third dataset was collected with identical settings except not in super resolution mode and with a pixel size of 1.047 Å/pix.

Cryo-EM data processing:

Cryo-EM movies (52,360 for INF2-actin; 24,201 for Dia1-actin) were imported into CryoSPARC v4.4 [43] and binned by two during patch motion correction, resulting in a pixel size of 1.08 Å. The third dataset was binned by 1.0315 using MotionCor2 [44] so that this data could be combined with the previous datasets. After patch contrast transfer function (CTF) estimation, micrographs were curated based on CTF fit, ice thickness, and manual inspection, yielding a final number of 49,225 and 22,140 movies for INF2 and Dia1, respectively.

For formins in the middle of F-actin, ~1,000 particles showing extra density on F-actin were manually picked and used to train a Topaz particle picking model [45]. Topaz-picked particles were extracted and subjected to reference-free 2D classification. Several iterations of Topaz particle picking and 2D classification yielded 3,824,735 and 570,665 initial particles of INF2 and Dia1, respectively. Particles were extracted with a pixel box size of 288, binned to 120 pixels, and subjected to further 2D classification to exclude featureless particles. Accepted particles were used to generate three ab-initio classes, including two resembling F-actin and one “junk” class. The volume from the best F-actin ab-initio class was used as the starting reference for heterogenous refinement with three classes, resulting in a bare F-actin class and two formin-bound classes. Particles from the formin-bound classes were subjected to non-uniform refinement, producing the initial maps of INF2 and Dia1 in the middle of F-actin.

For INF2, the particles in the initial map were subjected to several rounds of 3D classification focused on the FH2 domains to increase occupancy. This led to multiple classes where one of the FH2s (mobile) adopted “up” or “down” states, whereas the other FH2 (static) remained in the same position. We also observed low-occupancy classes where the mobile FH2 occupied intermediate positions between the up and down states. Particles belonging to the up and down states were separated and subjected to non-uniform refinement to produce separate maps of each state. Additional rounds of 3D classifications were performed focusing on the static and the mobile FH2s separately to increase their occupancy within both states. Non-uniform refinement was used to obtain final consensus maps containing 493,960 particles for the up state and 357,612 particles for the down state. For Dia1 in the middle, a similar procedure resulted in a consensus map containing 67,017 particles in a single state, distinct from both states of INF2.

For both INF2 and Dia1 at the barbed end, ~2,000 filament ends were manually picked and used to train Topaz as described above. The initial numbers of Topaz-picked particles were 2,035,152 and 88,114 for INF2 and Dia1, respectively. Particles were extracted with a pixel box size of 384, binned to 120 pixels, and subjected to further 2D classification to exclude particles that did not contain F-actin. Accepted particles were used to generate three ab-initio classes, including a barbed end, middle, and junk classes. Particles belonging to the barbed end and middle classes were used in multiple rounds of heterogeneous refinement to exclude non-barbed end particles. Barbed end particles were combined and subjected to non-uniform refinement. This map contained particles where the FH2s were misaligned, i.e. aligned with the wrong FH2 on the opposite long-pitch helix and shifted by one actin protomer. These particles were subjected to 3D classification focused on the misaligned FH2, which revealed that misalignment was due to some particles being shifted towards the pointed end by one actin protomer. These particles were re-centered and re-extracted such that all the ends were in register, which also realigned the FH2s.

For INF2, the resulting particle stack (~300,000 particles) was subjected to non-uniform refinement, yielding a map with poor density for the FH2 closest to the barbed end (leading FH2). These particles were subjected to further 3D classification focusing on the leading FH2, resulting in some classes containing both FH2s and some containing strong leading FH2 density but poor trailing FH2 density, and extra density that could not be assigned to the FH2s nor the barbed end. Particles belonging to the two-FH2 classes were combined and subjected to further 3D classification to increase occupancy of the FH2s, yielding a final map containing 169,402 particles. Particles belonging to classes with strong leading FH2 density were combined and subjected to 3D classification focusing on the unassigned density. This resulted in classes containing profilin-actin, and one class containing actin alone. Particles belonging to each class were separated and subjected to non-uniform refinements, resulting in the final consensus maps of INF2 with incoming profilin-actin (52,040 particles) and incoming actin (27,770 particles). Both structures were subjected to several rounds of 3D classification focusing on the trailing FH2 to improve its occupancy. A similar strategy resulted in a single consensus map of Dia1 at the barbed end.

For INF2 at the middle and barbed end of F-actin, 3D classification with masks focused on weak density corresponding to the WH2 domain bound to the actin subunits immediately

above the FH2s was performed. Particles belonging to subclasses with enriched WH2 density were combined into a consensus refinement.

For INF2 at the middle of F-actin, local refinements focusing on the static FH2, mobile FH2, and F-actin were performed for both the up and down states. At the barbed end, only the F-actin portion of the INF2 maps were subjected to local refinement. No local refinement was performed on maps of Dia1. Locally refined maps were combined to obtain the final composite maps used in refinement.

The orientation distribution efficiency scores of the cryo-EM maps were determined with the program cryoEF (v1.1.0) [46]. The FSC curves, directional orientation, power spectra, and sphericity scores were calculated using the 3DFSC server (https://3dfsc.salk.edu).

Model refinement:

Model building and refinement were performed with the programs Coot [47] and Phenix [48], respectively. For all the structures, initial formin models were obtained using AlphaFold [28], fit to the maps as rigid bodies, while allowing for inter-domain motions. The starting models of F-actin and profilin-actin were form PDB codes 8F8P and 2PAV, respectively. The FH2 domains were rigid-body fitted into the cryo-EM map as three separate blocks (knob, coiled-coil, lasso-post (Extended Data Fig. 1). The stereochemistry and fit were optimized using real space refinement in Phenix. Figures were prepared with the programs PyMOL (Schrodinger, LLC) and ChimeraX [49]. Final model quality and refinement statistics are given in Extended Data Tables 1–2.

Extended Data

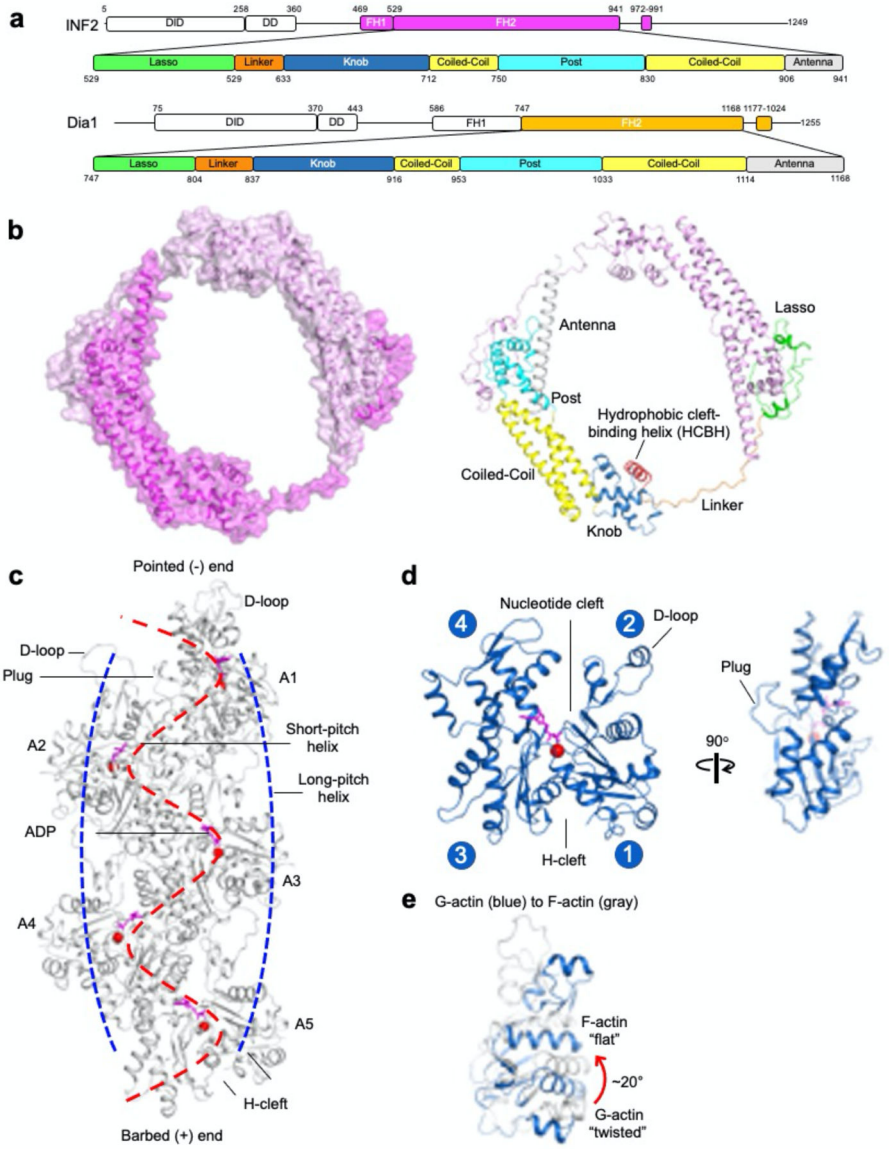

Extended Data Fig. 1 |. Definitions and nomenclatures used.

(a) Domain diagrams of INF2 and Dia1, with zooms defining sub-domains within the FH2 domain. **(b)** The FH2 dimer forms a ring-like structure mediated by head-to-tail lasso-post interactions (left). FH2 subdomains colored as in part a (right). The newly-defined HCBH is highlighted in red. **(c)** Actin filament (PDB code: 8F8P) indicating short and long-pitch helices, pointed and barbed ends, plug, H-cleft, and D-loop. **(d)** Two perpendicular views of the actin monomer (PDB code: 1J6Z) with subdomains 1–4 labeled in blue circles. The H-cleft, nucleotide cleft, D-loop, and plug are indicated. **(e)** G- (blue, twisted) to F-actin (gray, flat) conformational transition, characterized by a 20° rotation of subdomains 1 and 2 relative to 3 and 4.

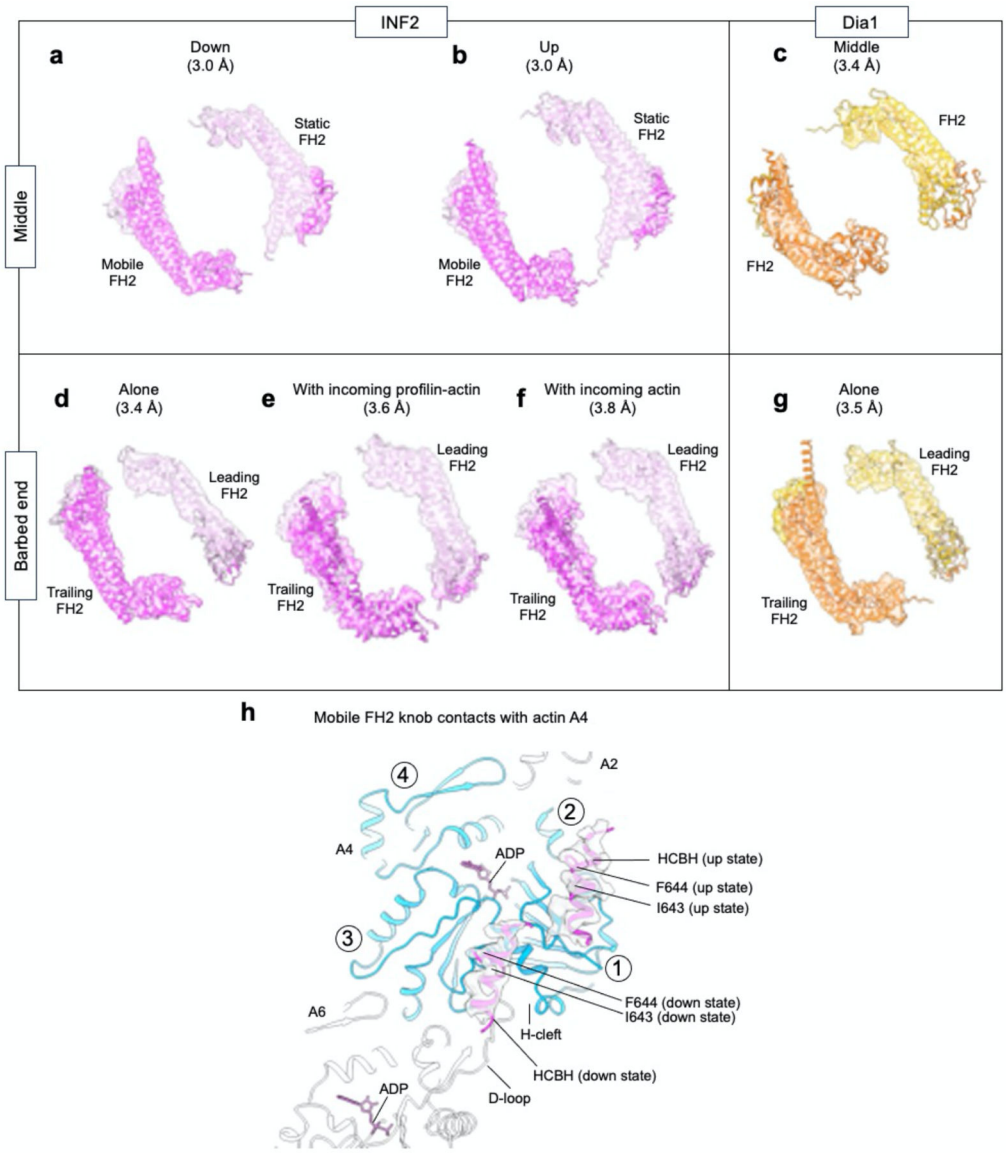

Extended Data Fig. 2 |. Cryo-EM maps around FH2 and HCBH.

(a-g) FH2 fit to the cryo-EM maps for the seven structures described here (as indicated). **(h)** HCBH of the mobile FH2 of INF2 fit to the cryo-EM map in the up and down mid-filament-bound states.

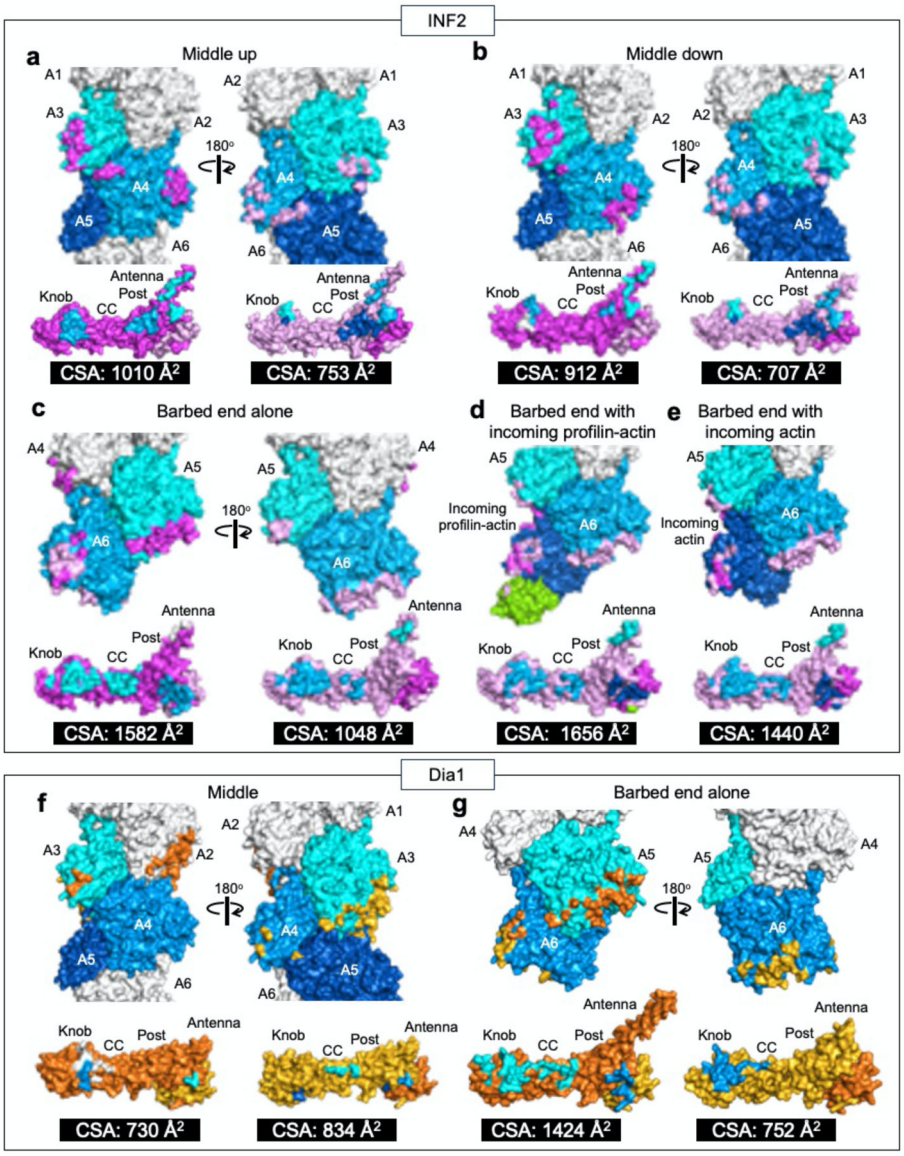

Extended Data Fig. 3 |. F-actin-FH2 contact surface areas.

(a-g) For each interaction, the contact area in F-actin is colored according to the interacting FH2. On the FH2 side, contact areas are colored cyan, marine blue, blue, and white depending on which actin subunit it contacts. Contact surface areas (given for each interaction in black boxes) were calculated using the server GetArea (https://curie.utmb.edu/getarea.html).

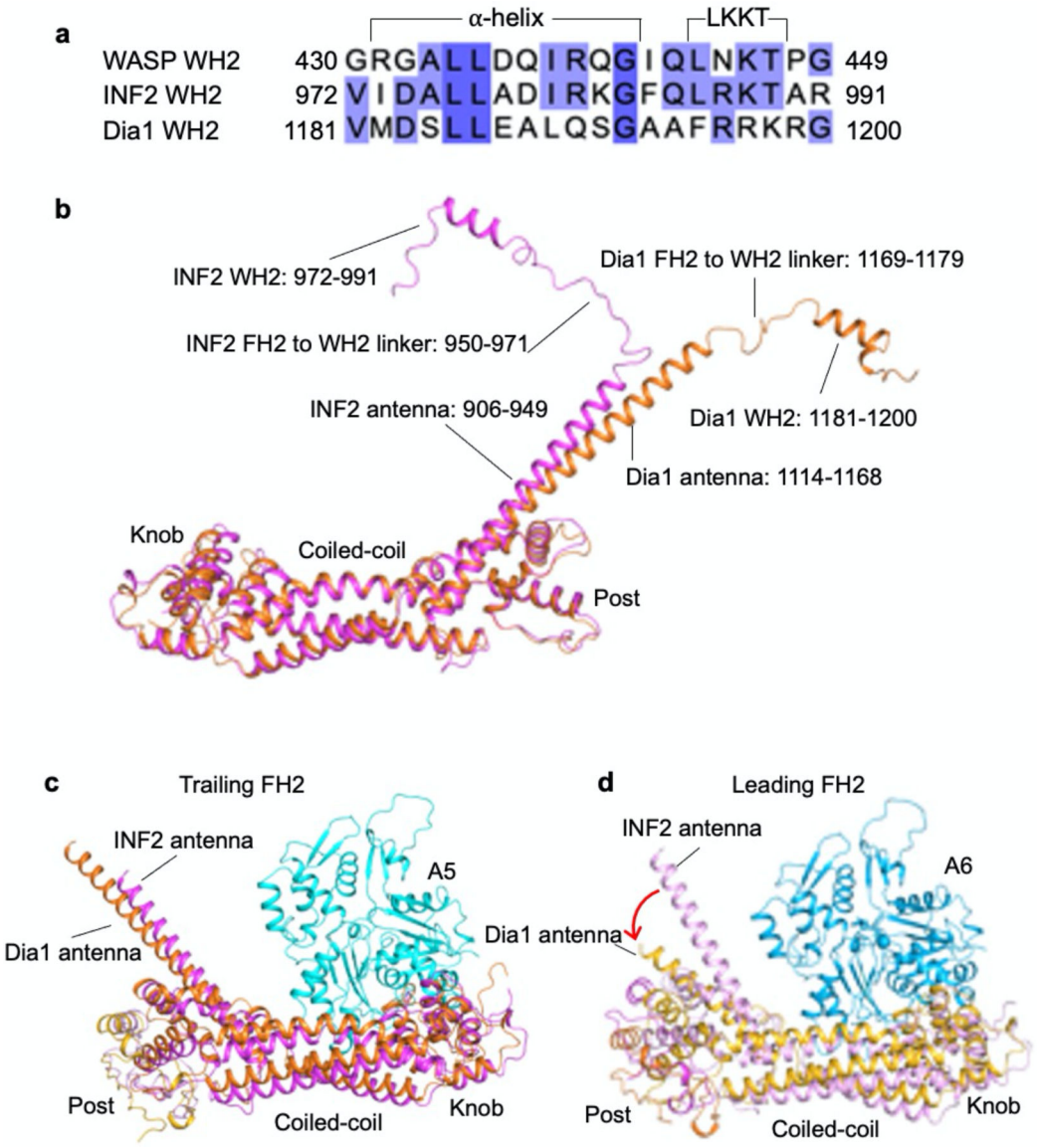

Extended data Fig. 4 |. Comparisons between INF2 and Dia1.

(a) Sequence alignment of WASP WH2 (UniProt code: P42768) with the WH2s of INF2 and Dia1. Note the absence of the LKKT motif in Dia1. **(b)** Superimposition of AlphaFold models of the FH2-WH2 regions of INF2 (632–991) and Dia1 (833–1200), highlighting differences in the length of the antennas and WH2-FH2 linkers. **(c-d)** Comparisons of the positions of the FH2s of INF2 (magenta) and Dia1 (orange) bound to A5 and A6 at the barbed end. The comparison is based on a superimposition of the corresponding actin subunits in the two structures.

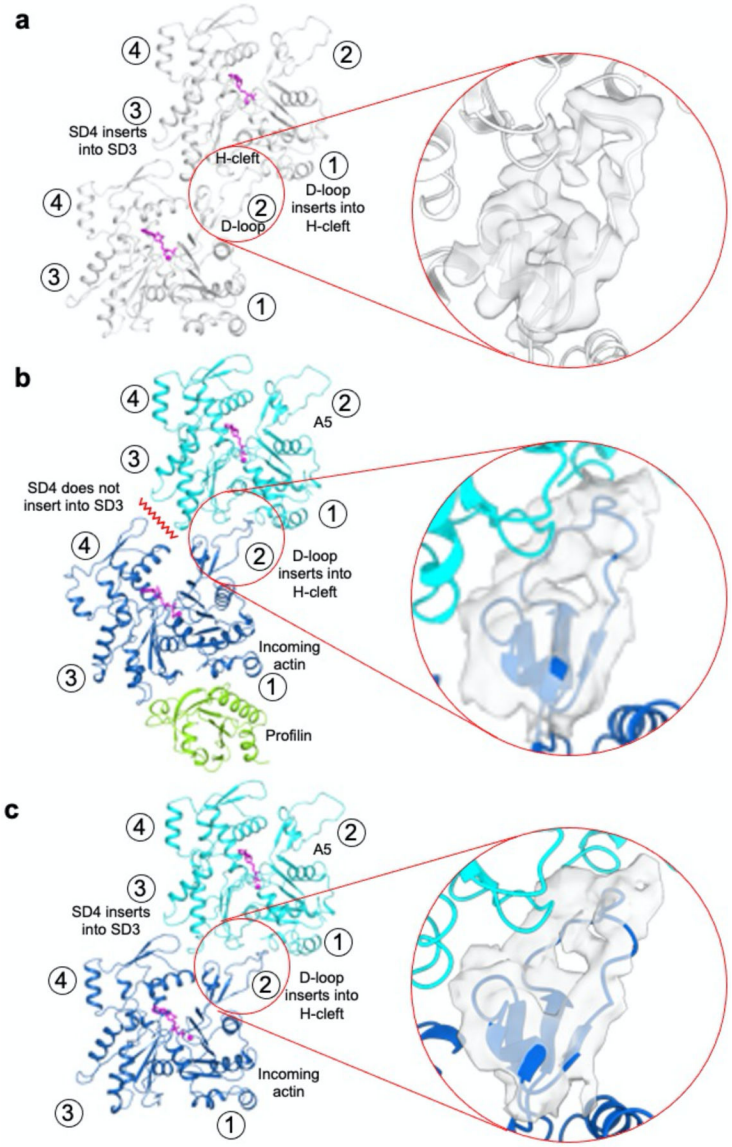

Extended Data Fig 5 |. Long-pitch interactions.

(a-c) Long-pitch interactions and corresponding cryo-EM maps of subdomain 2 in F-actin **(a)**, incoming profilin-actin **(b)** and incoming actin **(c)**. In all the structures, the D-loop inserts into the H-cleft of the subunit above. However, for the incoming monomer (blue), subdomain 4 contacts subdomain 3 of A5 only after a 14° rotation and the G- to F-actin transition (see also Fig. 3e–f in the main text).

Extended Data Table 1:

Cryo-EM data collection, refinement, and validation statistics for INF2

	Middle up (EMDB-44026) (PDB 9B03)	Middle down (EMDB-44045) (PDB 9B0K)	Barbed end (EMDB-44012) (PDB 9AZ4)	Barbed end with incoming profilin-actin (EMDB-44018) (PDB 9AZP)	Barbed end with incoming actin (EMDB-44019) (PDB 9AZQ)
Data collection and processing					
Magnification	81,000	81,000	81,000	81,000	81,000
Voltage (kV)	300	300	300	300	300
Electron exposure (e–/Å^2)	UPenn: 44 NCCAT-1: 52 NCCAT-2: 55	UPenn: 44 NCCAT-1: 52 NCCAT-2: 55	UPenn: 44 NCCAT-1: 52 NCCAT-2: 55	UPenn: 44 NCCAT-1: 52 NCCAT-2: 55	UPenn: 44 NCCAT-1: 52 NCCAT-2: 55
Defocus range (μm)	−0.5 to −2.5 um	−0.5 to −2.5 um	−0.5 to −2.5 um	−0.5 to −2.5 um	−0.5 to −2.5 um
Pixel size (Å)	0.54	0.54	0.54	0.54	0.54
Symmetry imposed	C1	C1	C1	C1	C1
Initial particle images (no.)	3,043,282	3,043,282	2,035,152	2,035,152	2,035,152
Final particle images (no.)	493,960	289,668	169,402	52,040	27,770
Map resolution (Å)	2.95	3.03	3.37	3.55	3.82
FSC threshold	0.143	0.143	0.143	0.143	0.143
Map resolution range (Å)	2.4 – 44.2	2.7 – 48.6	3.0 – 51.0	2.3 – 57.0	3.5 – 62.4
Refinement					
Initial model used (PDB code)	8F8P (F-actin) AlphaFold (INF2)	8F8P (F-actin) AlphaFold (INF2)	8F8P (F-actin) AlphaFold (INF2)	8F8P (F-actin) AlphaFold (INF2) 2PAV (profilin-actin)	8F8P (F-actin) AlphaFold (INF2)
Model resolution (Å)	3.4	3.3	3.8	3.9	4.2
FSC threshold	0.5	0.5	0.5	0.5	0.5
Map sharpening *B* factor (Å^2)	103.4	101.4	92.0	64.3	54.5
Model composition					
Non-hydrogen atoms	23,898	23,869	23,867	27,676	26,626
Protein residues	3,020	3,016	3,015	3,502	3,363
Ligands	ADP: 6, MG: 6	ADP: 6, MG: 6	ADP: 6, MG: 6	ADP: 6, MG: 7, ATP: 1	ADP: 7, MG: 7
B factors (Å^2)					
Protein (min / max / mean)	38.72 / 436.54 / 167.39	68.14 / 342.01 / 172.44	86.89 / 609.57 / 214.93	71.69 / 449.24 / 171.44	113.32 / 1014.39 / 387.27
Ligand (min / max / mean)	51.97 / 141.98 / 104.12				

	Middle up (EMDB-44026) (PDB 9B03)	Middle down (EMDB-44045) (PDB 9B0K)	Barbed end (EMDB-44012) (PDB 9AZ4)	Barbed end with incoming profilin-actin (EMDB-44018) (PDB 9AZP)	Barbed end with incoming actin (EMDB-44019) (PDB 9AZQ)
R.m.s. deviations					
Bond lengths (Å)	0.005 (0)	0.005 (0)	0.007 (0)	0.006 (1)	0.006 (0)
Bond angles (°)	0.962 (24)	0.926 (23)	1.054 (26)	1.055 (34)	1.074 (32)
Validation					
MolProbity score	1.13	1.02	1.29	1.16	1.25
Clashscore	1.91	1.37	2.65	1.87	2.19
Poor rotamers (%)	0.00	0.07	0.03	0.03	0.00
Ramachandran plot					
Favored (%)	97.01	97.14	96.40	96.67	96.27
Allowed (%)	2.99	2.79	3.57	3.30	3.73
Disallowed (%)	0.00	0.07	0.03	0.03	0.00

Extended Data Table 2:

Cryo-EM data collection, refinement, and validation statistics for Dia1

	Middle (EMDB-44135) (PDB 9B3D)	Barbed end (EMDB-44099) (PDB 9B27)
Data collection and processing		
Magnification	81,000	81,000
Voltage (kV)	300	300
Electron exposure (e–/Å^2)	UPenn: 42	UPenn: 42
Defocus range (μm)	−0.5 to −2.5 um	−0.5 to −2.5 um
Pixel size (Å)	0.54	0.54
Symmetry imposed	C1	C1
Initial particle images (no.)	570,665	88,114
Final particle images (no.)	59.861	36,931
Map resolution (Å)	3.41	3.51
FSC threshold	0.143	0.143
Map resolution range (Å)	2.33 – 55.5	3.16 – 56.9
Refinement		
Initial model used (PDB code)	8F8P (F-actin) AlphaFold (Dia1)	8F8P (F-actin) AlphaFold (Dia1)
Model resolution (Å)	3.81	3.94
FSC threshold	0.5	0.5
Map sharpening *B* factor (Å^2)	−73.1	−46.4
Model composition		

	Middle (EMDB-44135) (PDB 9B3D)	Barbed end (EMDB-44099) (PDB 9B27)
Non-hydrogen atoms	23,621	23,828
Protein residues	2,967	2,991
Ligands	ADP: 6, MG: 6	ADP: 6, MG: 6
B factors (Å^2)		
Protein (min / max / mean)	46.29 / 413.56 / 139.35	111.52 / 977.84 / 217.29
Ligand (min / max / mean)	50.26 / 11.95 / 84.22	12.40 / 152.65 / 137.77
R.m.s. deviations		
Bond lengths (Å)	0.005 (1)	0.004 (0)
Bond angles (°)	0.874 (11)	0.810 (12)
Validation		
MolProbity score	1.24	1.23
Clashscore	2.11	2.17
Poor rotamers (%)	0.10	0.00
Ramachandran plot		
Favored (%)	96.17	96.44
Allowed (%)	3.72	3.56
Disallowed (%)	0.10	0.00

Supplementary Material

Refer to Web version on PubMed Central for supplementary material.

Acknowledgments:

We thank Henry Higgs for providing the INF2 and Dia1 genes. This study was supported by National Institutes of Health (NIH) grants R01 GM073791 and RM1 GM136511 to R.D. and T32 AR053461 to N.J.P. Data collection was supported by the Electron Microscopy Resource Lab (EMRL) and The Beckman Center for Cryo-Electron Microscopy, University of Pennsylvania (Research Resource Identifier SCR_022375), and the National Center for CryoEM Access and Training (NCCAT) through NIH grant U24 GM129539.

Data availability:

Molecular models and cryo-EM density maps have been deposited with the following accession codes:

INF2 middle up (PDB code: 9B03; EMDB codes: EMD-44026, EMD-44020, EMD-44022, EMD-44023, EMD-44024, EMD-44025, EMD-44948)

INF2 middle down (PDB code: 9B0K; EMDB codes: EMD-44045, EMD-44027, EMD-44030, EMD-44031, EMD-44032, EMD-44033, EMD-44943)

Dia1 middle (PDB code: 9B3D; EMDB codes: EMD-44135)

INF2 at the barbed end (PDB code: 9AZ4; EMDB codes: EMD-44012, EMD-44009, EMD-44010, EMD-44011, EMD-44950, EMD-44951)

Dia1 barbed end (PDB code: 9B27; EMDB code: EMD-44099)

INF2 with incoming profilin-actin (PDB code: 9AZP; EMDB codes: EMD-44018, EMD-44956, EMD-44958)

INF2 with incoming actin (PDB code: 9AZQ; EMDB codes: EMD-44019, EMD-44973, EMD-44972).

Previously published structures used in model building (PDB codes: 2PAV and 8F8P).

References and notes

1. Breitsprecher D & Goode BL Formins at a glance. J Cell Sci 126, 1–7, doi:10.1242/jcs.107250 (2013). [PubMed: 23516326]
2. Valencia DA & Quinlan ME Formins. Curr Biol 31, R517–R522, doi:10.1016/j.cub.2021.02.047 (2021). [PubMed: 34033783]
3. Romero S et al. Formin is a processive motor that requires profilin to accelerate actin assembly and associated ATP hydrolysis. Cell 119, 419–429 (2004). [PubMed: 15507212]
4. Kovar DR, Harris ES, Mahaffy R, Higgs HN & Pollard TD Control of the assembly of ATP- and ADP-actin by formins and profilin. Cell 124, 423–435 (2006). [PubMed: 16439214]
5. Otomo T et al. Structural basis of actin filament nucleation and processive capping by a formin homology 2 domain. Nature 433, 488–494 (2005). [PubMed: 15635372]
6. Paul AS & Pollard TD Review of the mechanism of processive actin filament elongation by formins. Cell Motil Cytoskeleton 66, 606–617 (2009). [PubMed: 19459187]
7. Thompson ME, Heimsath EG, Gauvin TJ, Higgs HN & Kull FJ FMNL3 FH2-actin structure gives insight into formin-mediated actin nucleation and elongation. Nat Struct Mol Biol 20, 111–118, doi:10.1038/nsmb.2462 (2013). [PubMed: 23222643]
8. Chhabra ES & Higgs HN INF2 Is a WASP homology 2 motif-containing formin that severs actin filaments and accelerates both polymerization and depolymerization. The Journal of biological chemistry 281, 26754–26767, doi:10.1074/jbc.M604666200 (2006). [PubMed: 16818491]
9. Gurel PS et al. INF2-mediated severing through actin filament encirclement and disruption. Curr Biol 24, 156–164, doi:10.1016/j.cub.2013.12.018 (2014). [PubMed: 24412206]
10. Gurel PS et al. Assembly and turnover of short actin filaments by the formin INF2 and profilin. J Biol Chem 290, 22494–22506, doi:10.1074/jbc.M115.670166 (2015). [PubMed: 26124273]
11. Korobova F, Ramabhadran V & Higgs HN An actin-dependent step in mitochondrial fission mediated by the ER-associated formin INF2. Science 339, 464–467, doi:10.1126/science.1228360 (2013). [PubMed: 23349293]
12. Higgs HN Formin proteins: a domain-based approach. Trends Biochem Sci 30, 342–353 (2005). [PubMed: 15950879]
13. Zimmermann D & Kovar DR Feeling the force: formin's role in mechanotransduction. Curr Opin Cell Biol 56, 130–140, doi:10.1016/j.ceb.2018.12.008 (2019). [PubMed: 30639952]
14. Labat-de-Hoz L & Alonso MA Formins in Human Disease. Cells 10, doi:10.3390/cells10102554 (2021).
15. Mullins RD, Bieling P & Fletcher DA From solution to surface to filament: actin flux into branched networks. Biophys Rev 10, 1537–1551, doi:10.1007/s12551-018-0469-5 (2018). [PubMed: 30470968]
16. Xu Y et al. Crystal structures of a Formin Homology-2 domain reveal a tethered dimer architecture. Cell 116, 711–723 (2004). [PubMed: 15006353]
17. Zigmond SH et al. Formin leaky cap allows elongation in the presence of tight capping proteins. Curr Biol 13, 1820–1823 (2003). [PubMed: 14561409]
18. Kovar DR, Kuhn JR, Tichy AL & Pollard TD The fission yeast cytokinesis formin Cdc12p is a barbed end actin filament capping protein gated by profilin. J Cell Biol 161, 875–887 (2003). [PubMed: 12796476]

19. Gould CJ et al. The formin DAD domain plays dual roles in autoinhibition and actin nucleation. Current biology : CB 21, 384–390, doi:10.1016/j.cub.2011.01.047 (2011). [PubMed: 21333540]
20. Quinlan ME, Hilgert S, Bedrossian A, Mullins RD & Kerkhoff E Regulatory interactions between two actin nucleators, Spire and Cappuccino. The Journal of cell biology 179, 117–128, doi:10.1083/jcb.200706196 (2007). [PubMed: 17923532]
21. Breitsprecher D et al. Rocket launcher mechanism of collaborative actin assembly defined by single-molecule imaging. Science 336, 1164–1168, doi:10.1126/science.1218062 (2012). [PubMed: 22654058]
22. Yamana N et al. The Rho-mDia1 pathway regulates cell polarity and focal adhesion turnover in migrating cells through mobilizing Apc and c-Src. Mol Cell Biol 26, 6844–6858 (2006). [PubMed: 16943426]
23. Brandt DT et al. Dia1 and IQGAP1 interact in cell migration and phagocytic cup formation. J Cell Biol 178, 193–200, doi:10.1083/jcb.200612071 (2007). [PubMed: 17620407]
24. Fessenden TB et al. Dia1-dependent adhesions are required by epithelial tissues to initiate invasion. J Cell Biol 217, 1485–1502, doi:10.1083/jcb.201703145 (2018). [PubMed: 29437785]
25. Brown EJ et al. Mutations in the formin gene INF2 cause focal segmental glomerulosclerosis. Nat Genet 42, 72–76, doi:10.1038/ng.505 (2010). [PubMed: 20023659]
26. Boyer O et al. INF2 mutations in Charcot-Marie-Tooth disease with glomerulopathy. N Engl J Med 365, 2377–2388, doi:10.1056/NEJMoa1109122 (2011). [PubMed: 22187985]
27. Ueyama T et al. Constitutive activation of DIA1 (DIAPH1) via C-terminal truncation causes human sensorineural hearing loss. EMBO Mol Med 8, 1310–1324, doi:10.15252/emmm.201606609 (2016). [PubMed: 27707755]
28. Jumper J et al. Highly accurate protein structure prediction with AlphaFold. Nature 596, 583–589, doi:10.1038/s41586-021-03819-2 (2021). [PubMed: 34265844]
29. Carman PJ, Barrie KR, Rebowski G & Dominguez R Structures of the free and capped ends of the actin filament. Science, eadg6812, doi:10.1126/science.adg6812 (2023).
30. Jaiswal R et al. The formin Daam1 and fascin directly collaborate to promote filopodia formation. Curr Biol 23, 1373–1379, doi:10.1016/j.cub.2013.06.013 (2013). [PubMed: 23850281]
31. Bombardier JP et al. Single-molecule visualization of a formin-capping protein 'decision complex' at the actin filament barbed end. Nat Commun 6, 8707, doi:10.1038/ncomms9707 (2015). [PubMed: 26566078]
32. Harris ES, Rouiller I, Hanein D & Higgs HN Mechanistic differences in actin bundling activity of two mammalian formins, FRL1 and mDia2. J Biol Chem 281, 14383–14392 (2006). [PubMed: 16556604]
33. Scott BJ, Neidt EM & Kovar DR The functionally distinct fission yeast formins have specific actin-assembly properties. Mol Biol Cell 22, 3826–3839, doi:10.1091/mbc.E11-06-0492 (2011). [PubMed: 21865598]
34. Ramabhadran V, Gurel PS & Higgs HN Mutations to the formin homology 2 domain of INF2 protein have unexpected effects on actin polymerization and severing. The Journal of biological chemistry 287, 34234–34245, doi:10.1074/jbc.M112.365122 (2012). [PubMed: 22879592]
35. Maufront J et al. Direct observation of the conformational states of formin mDia1 at actin filament barbed ends and along the filament. Mol Biol Cell 34, ar2, doi:10.1091/mbc.E22-10-0472 (2023). [PubMed: 36383775]
36. Chereau D et al. Actin-bound structures of Wiskott-Aldrich syndrome protein (WASP)-homology domain 2 and the implications for filament assembly. Proceedings of the National Academy of Sciences of the United States of America 102, 16644–16649, doi:10.1073/pnas.0507021102 (2005). [PubMed: 16275905]
37. Dominguez R The WH2 Domain and Actin Nucleation: Necessary but Insufficient. Trends Biochem Sci 41, 478–490, doi:10.1016/j.tibs.2016.03.004 (2016). [PubMed: 27068179]
38. Zsolnay V, Katkar HH, Chou SZ, Pollard TD & Voth GA Structural basis for polarized elongation of actin filaments. Proc Natl Acad Sci U S A 117, 30458–30464, doi:10.1073/pnas.2011128117 (2020). [PubMed: 33199648]
39. Oda T, Iwasa M, Aihara T, Maeda Y & Narita A The nature of the globular- to fibrous-actin transition. Nature 457, 441–445 (2009). [PubMed: 19158791]

40. Pollard TD Actin and Actin-Binding Proteins. Cold Spring Harb Perspect Biol 8, doi:10.1101/cshperspect.a018226 (2016).
41. Oosterheert W et al. Molecular mechanism of actin filament elongation by formins. Science 384, eadn9560, doi:10.1126/science.adn9560 (2024). [PubMed: 38603491]
42. Ferron F, Rebowski G, Lee SH & Dominguez R Structural basis for the recruitment of profilin-actin complexes during filament elongation by Ena/VASP. The EMBO journal 26, 4597–4606, doi:10.1038/sj.emboj.7601874 (2007). [PubMed: 17914456]

Additional references

43. Punjani A, Rubinstein JL, Fleet DJ & Brubaker MA cryoSPARC: algorithms for rapid unsupervised cryo-EM structure determination. Nat Methods 14, 290–296, doi:10.1038/nmeth.4169 (2017). [PubMed: 28165473]
44. Zheng SQ et al. MotionCor2: anisotropic correction of beam-induced motion for improved cryo-electron microscopy. Nat Methods 14, 331–332, doi:10.1038/nmeth.4193 (2017). [PubMed: 28250466]
45. Bepler T et al. Positive-unlabeled convolutional neural networks for particle picking in cryo-electron micrographs. Nat Methods 16, 1153–1160, doi:10.1038/s41592-019-0575-8 (2019). [PubMed: 31591578]
46. Naydenova K & Russo CJ Measuring the effects of particle orientation to improve the efficiency of electron cryomicroscopy. Nat Commun 8, 629, doi:10.1038/s41467-017-00782-3 (2017). [PubMed: 28931821]
47. Casanal A, Lohkamp B & Emsley P Current developments in Coot for macromolecular model building of Electron Cryo-microscopy and Crystallographic Data. Protein Sci 29, 1069–1078, doi:10.1002/pro.3791 (2020). [PubMed: 31730249]
48. van Zundert GCP, Moriarty NW, Sobolev OV, Adams PD & Borrelli KW Macromolecular refinement of X-ray and cryoelectron microscopy structures with Phenix/OPLS3e for improved structure and ligand quality. Structure 29, 913–921 e914, doi:10.1016/j.str.2021.03.011 (2021). [PubMed: 33823127]
49. Pettersen EF et al. UCSF ChimeraX: Structure visualization for researchers, educators, and developers. Protein Sci 30, 70–82, doi:10.1002/pro.3943 (2021). [PubMed: 32881101]

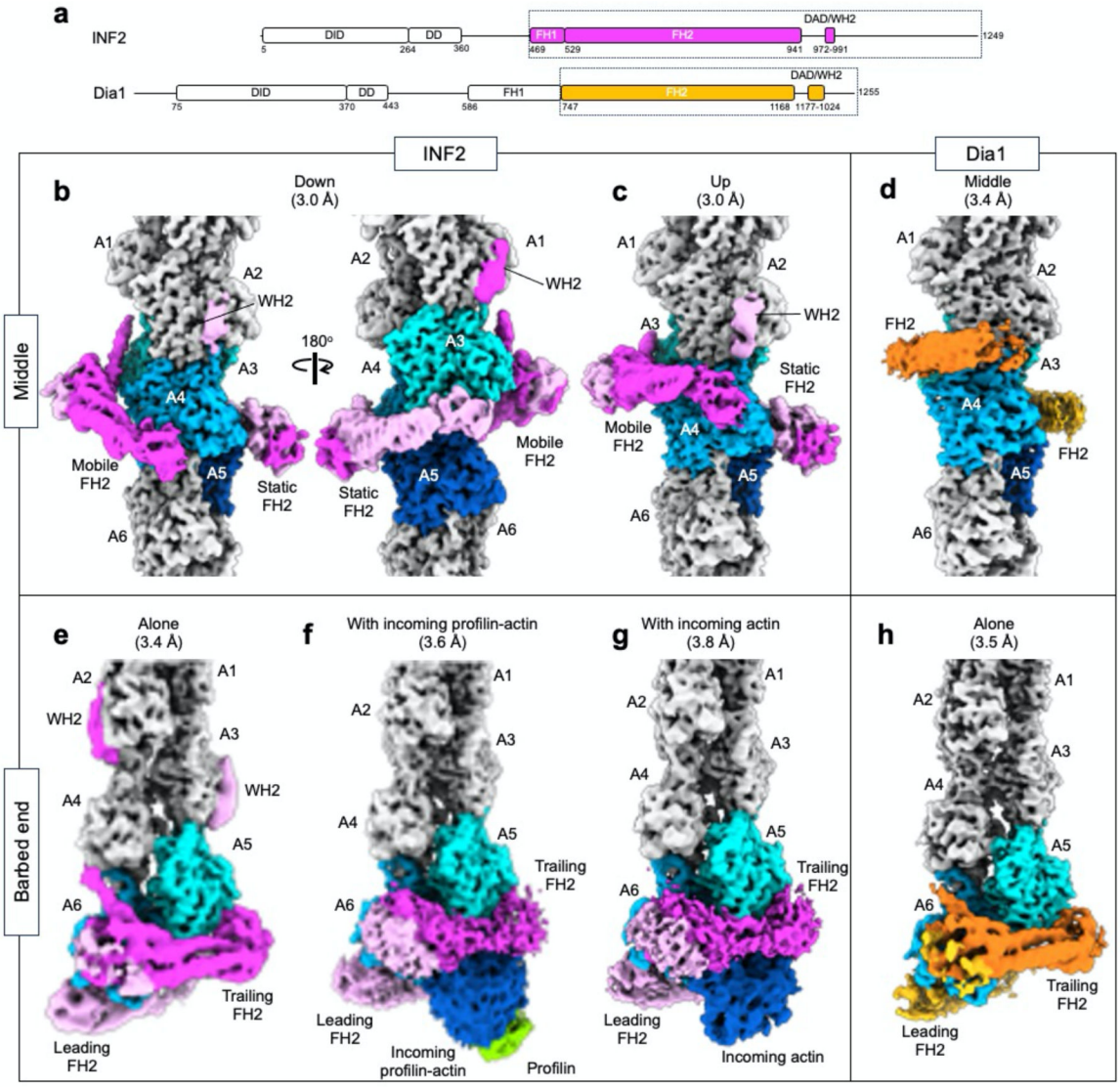

Fig. 1 |. Cryo-EM structures of INF2 and Dia1 bound to F-actin.

(a) Domain diagrams of human INF2 and mouse Dia1. Constructs used here are indicated by a dotted black outline. DID, diaphanous inhibitory domain; DD, dimerization domain; FH1 and FH2, formin-homology 1 and 2 domains, DAD, diaphanous autoregulatory domain; WH2, WASP-homology-2 domain. **(b-h)** Seven structural states of INF2 (two shades of magenta) and Dia1 (two shades of orange) bound to the middle and barbed end of F-actin, as indicated. Actin subunits are colored gray or different shades of blue according to their positions relative to the formins.

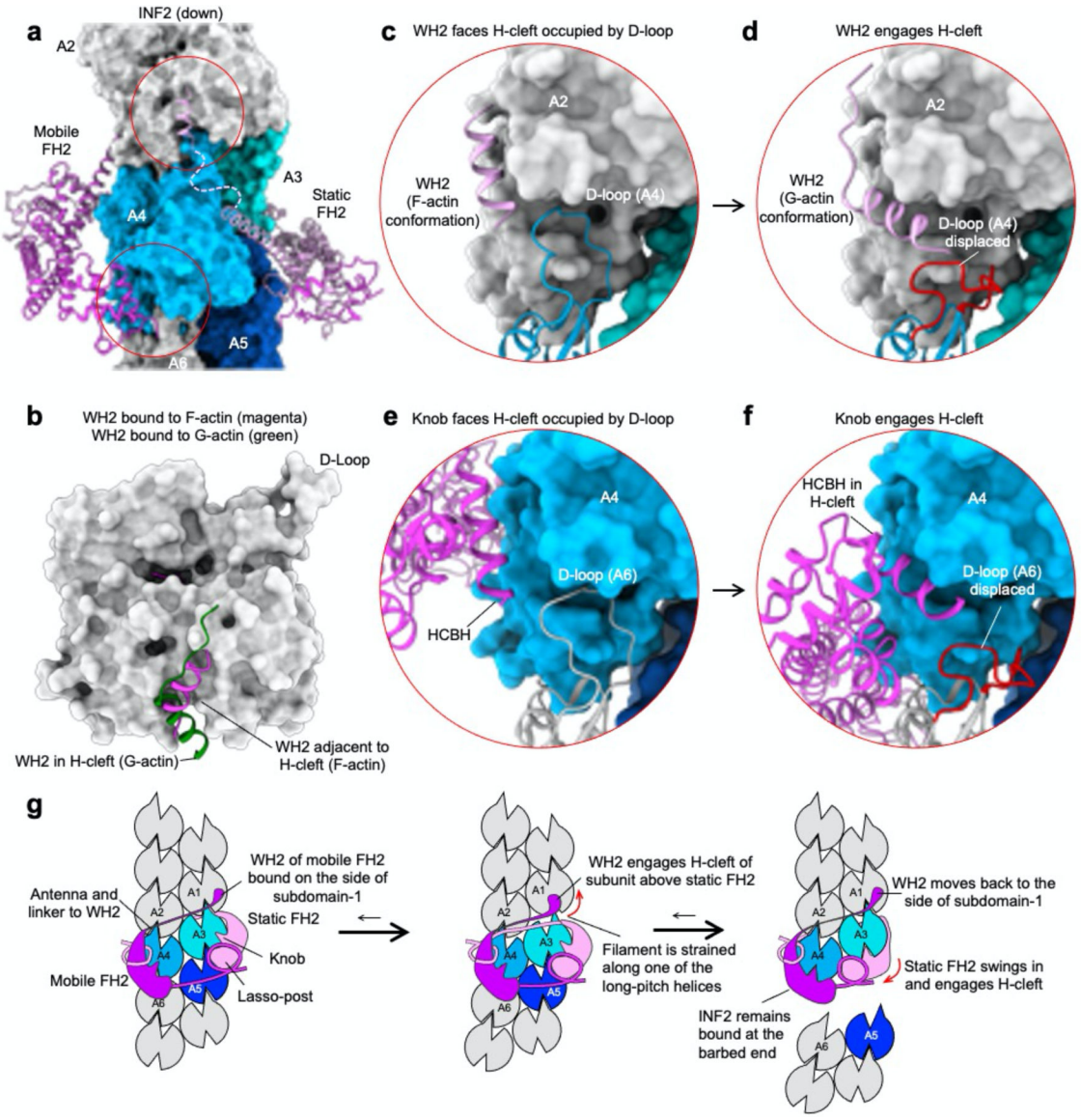

Fig. 2 |. Hand-over-hand severing mechanism.

(a) INF2 bound to the middle of F-actin (down state). **(b)** Interaction of the WH2 of INF2 with G-actin (green, AlphaFold prediction) vs. F-actin (magenta, from part a). **(c)** Close-up from part a, showing the WH2 of INF2 bound to the side of the H-cleft of A2, which is occupied by the D-loop of A4. **(d)** Thermal motions of the D-loop are proposed to allow the WH2 to competitively bind to its preferred site in the H-cleft, displacing the D-loop and destabilizing contacts along the long-pitch helix. **(e)** Close-up from part a, showing INF2's HCBH bound to the side of the H-cleft of A4, which is occupied by the D-loop of A6. **(f)** Following destabilization of the long-pitch helix by the WH2, HCBH is proposed to opportunistically bind to its preferred site in the H-cleft, displacing the D-loop. This sequence of events can occur on either side of F-actin, leading to severing. **(g)** Cartoon representation of key steps in the proposed severing mechanism. See also Supplementary Video 2.

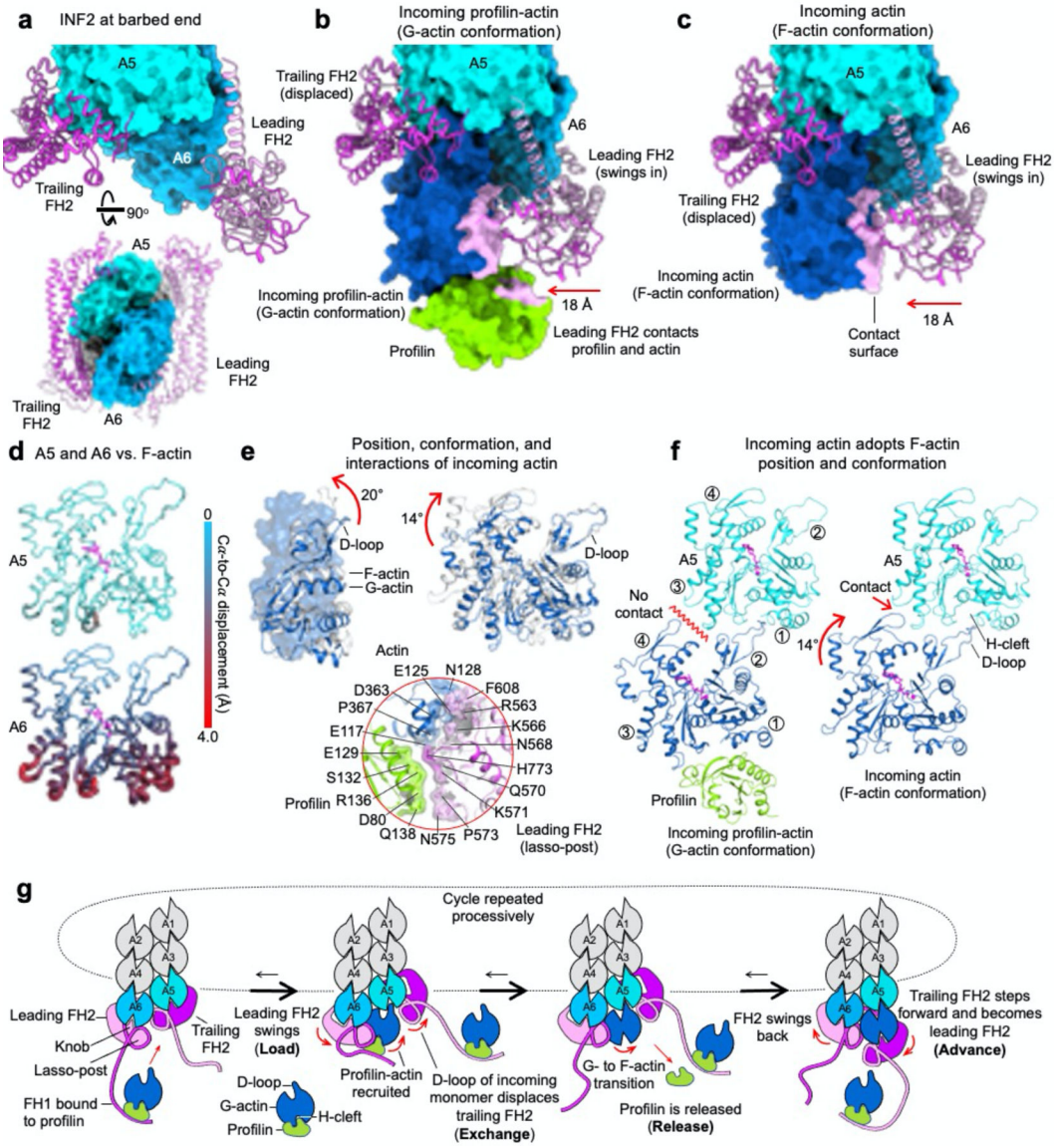

Fig. 3 |. LERA elongation mechanism.

(a) Two perpendicular views of INF2 at the barbed end. **(b)** INF2 at the barbed end with incoming profilin-actin (green and blue). The monomer has a G-actin conformation. Relative to its position at the barbed end, the lasso-post of the leading FH2 moves inward ~18 Å (red arrow) and interacts with both profilin and actin (pink surface). The trailing FH2 is displaced from the H-cleft of A5 by the D-loop of the incoming monomer. **(c)** INF2 at the barbed end with incoming actin. The monomer has adopted the F-actin conformation and profilin has been released. The FH2s occupy the same position as in part b. **(d)** Cartoon putty representation of A5 and A6 from part a, colored and rendered according to Ca-to-Ca displacement (side bar) from F-actin. **(e)** The monomer in the incoming profilin-actin structure (part b) is in the G-actin conformation (left) and rotated 14° relative to its final position in F-actin (right). Interaction of the lasso-post of the leading FH2 with profilin-actin (bottom). **(f)** Long-pitch contacts of the monomer in the incoming profilin-actin (left) and

actin (right) structures. Actin subdomains are indicated by circled numbers (1 to 4). In both structures, the D-loop inserts into the H-cleft of A5, whereas subdomain 4 contacts subdomain 3 of A5 only after the 14° rotation and G- to F-actin transition (part e). **(g)** Cartoon representation of key steps in the proposed elongation mechanism. See also Supplementary Video 4.